PLEASE CITE THIS ARTICLE AS DOI: 10.1063/5.0128842

## **Voltage Modulated Magnetic Anisotropy of Rare Earth Iron Garnet Thin** Films on a Piezoelectric Substrate

Miela J. Gross<sup>1</sup>, Walid A. Misba<sup>2</sup>, Kensuke Hayashi<sup>3</sup>, Dhritiman Bhattacharya<sup>4</sup>, Daniel B. Gopman<sup>5</sup>, Jayasimha Atulasimha<sup>2</sup>, Caroline A. Ross<sup>3\*</sup>

<sup>1</sup>Department of Electrical Engineering and Computer Science, Massachusetts Institute of Technology, Cambridge, Massachusetts, 02139, USA

<sup>2</sup>Department of Mechanical and Nuclear Engineering, Virginia Commonwealth University, Richmond, Virginia, 23284, USA

<sup>3</sup>Department of Materials Science and Engineering, Massachusetts Institute of Technology, Cambridge, Massachusetts, 02139, USA

<sup>4</sup>Department of Physics, Georgetown University, Washington, District of Columbia, 20057, USA <sup>5</sup>Materials Science and Engineering Division, NIST, Gaithersburg, Maryland, 20899-8552, USA

## **Abstract**

Voltage-tuning of the magnetic anisotropy is demonstrated in ferrimagnetic insulating rare earth iron garnets on a piezoelectric substrate, (011)-oriented PMN-PT. A yttrium-substituted dysprosium iron garnet (YDyIG) film 42 nm thick is grown via pulsed laser deposition followed by a rapid thermal anneal to crystallize the garnet into ≈5 µm diameter grains. The polycrystalline film is magnetically isotropic in the film plane, with total anisotropy dominated by shape and magnetoelastic contributions. Application of an electric field perpendicular to the substrate breaks the in-plane symmetry leading to the development of an in-plane easy axis along [100] and an intermediate axis along  $[01\overline{1}]$ . The results are explained in terms of the piezoelectric remanent strain caused by poling the substrate, which is transferred to the YDyIG and modulates the magnetoelastic anisotropy.

## **Main Text**

Rare earth iron garnets (REIGs) are a class of cubic ferrimagnetic insulators with composition RE<sub>3</sub>Fe<sub>5</sub>O<sub>12</sub> which have a wide range of tunable properties and hold interest for applications in spintronic, magnonic and neuromorphic computing devices<sup>1-4</sup>. The low to moderate damping of iron garnets<sup>5–7</sup> allows for fast spin wave dynamics and high domain wall speeds as demonstrated in thulium iron garnet<sup>8,9</sup> and bismuth substituted yttrium iron garnet<sup>10-12</sup>. In addition, a Dzyaloshinskii-Moriya interaction (DMI) originating from the garnet/substrate interface has been reported<sup>13-16</sup>, stabilizing homochiral domain walls. REIGs can be grown with perpendicular magnetic anisotropy (PMA) due to magnetoelastic<sup>7,17,18</sup> or growth induced anisotropy<sup>19</sup>. PMA provides a favorable configuration for manipulating the magnetization through spin orbit torque via a current in an adjacent spin-Hall conductor layer, a more energy-efficient method than conventional spin transfer torque<sup>20</sup>.

<sup>\*</sup>To whom correspondence should be addressed. E-mail: caross@mit.edu

PLEASE CITE THIS ARTICLE AS DOI: 10.1063/5.0128842

Magnetoelastic anisotropy is determined by the strain state and magnetoelastic properties of the REIG, expressed by the magnetostriction coefficients  $\lambda_{100}$  and  $\lambda_{111}$  or the magnetoelastic moduli  $B_1$  and  $B_2$  which describe the response in the <100> and <111> directions respectively. Magnetoelastic anisotropy favors out of plane (OP) magnetization for a film with a compressive in-plane (IP) strain state and positive magnetostriction coefficient, or tensile IP strain and a negative magnetostriction coefficient<sup>21,22</sup>. The strain in garnet films originates from lattice mismatch<sup>23,24</sup> or thermal expansion mismatch<sup>18,25</sup> between the film and substrate. This implies that active modulation of the anisotropy can be accomplished by depositing the film on a piezoelectric substrate and applying strain with an applied voltage.

There have been several demonstrations of voltage-tuning of magnetic properties in a magnetoelastic/piezoelectric composite, including bulk bonded composites  $^{26,27}$ , and magnetic films grown directly on a piezoelectric substrate  $^{28}$ . For example, changes in anisotropy have been reported for films and nanostructures of Ni $^{29-31}$ , Co $^{32-34}$ , CoFeB $^{35}$ , SmCo $^{36}$ , and Fe $_4$ N $^{37}$  deposited on PMN-PT [(PbMg0.33Nb0.67O3)1-x(PbTiO3)x] substrates. Oxide films including magnetite  $^{38}$  and YIG $^{39-41}$  have also been grown on piezoelectric substrates and their properties modulated via strain. The generation of magnons in YIG under an oscillating strain state, as well as spin transport in YIG/Cr $_2$ O $_3$  has been investigated  $^{42-44}$ . The damping of YIG has also been modified using voltage-induced strain in YIG/PMN-PT heterostructures.  $^{45}$  However, voltage-induced anisotropy modulation has yet to be demonstrated in rare-earth iron garnet films grown on a piezoelectric substrate.

Here we show that modulating the strain in a REIG film by applying an electric field to the PMN-PT substrate leads to a variation in the anisotropy. This change in anisotropy can be related to the biaxial remanent strain imposed by poling the substrate. The REIG is yttrium-substituted dysprosium iron garnet (Y<sub>1.25</sub>Dy<sub>1.75</sub>Fe<sub>5</sub>O<sub>12</sub> or YDyIG) grown on a (011)-oriented PMN-PT substrate coated with a buffer layer (5 nm of silica), which prevents the formation of epitaxial orthoferrite phases<sup>46,47</sup>. YDyIG was selected because its magnetostriction coefficients have the same sign and are larger than those of YIG, leading to a larger magnetoelastic anisotropy for polycrystalline YDyIG than that of polycrystalline YIG films. Substitution of Y lowers the coercivity and anisotropy, to enable larger strain-induced changes in anisotropy to be obtained. The piezoelectric substrate is poled at different voltages to induce varying remanent strain states in the film, and the magnetic anisotropy of the garnet is analyzed. These results give insights into ferrimagnetic/piezoelectric heterostructures with adjustable anisotropy that may be useful for neuromorphic and spintronic device applications.

Our prior work has shown that polycrystalline DylG (Dy<sub>3</sub>Fe<sub>5</sub>O<sub>12</sub>) grown on Si exhibits PMA<sup>25,48</sup>. Film growth and characterization was carried out as described in Supplementary Materials. The as-deposited amorphous film is crystallized by RTA and develops IP tensile strain on cooling due to the larger thermal expansion of garnets compared to Si. Both magnetostriction coefficients of DylG,  $\lambda_{100}$  and  $\lambda_{111}$ , are negative. This ensures that any of the randomly oriented grains in the polycrystalline film will have the same sign of magnetoelastic anisotropy. Polycrystalline DylG has a magnetostriction coefficient that can be approximated<sup>49</sup> as  $\lambda_s = 0.4 \ \lambda_{100} + 0.6 \ \lambda_{111} = -8.54 \times 10^{-6}$ .

PLEASE CITE THIS ARTICLE AS DOI: 10.1063/5.0128842

At room temperature DyIG/Si has a high coercivity, e.g., 200 mT in our earlier work<sup>25</sup> and a low saturation magnetization ( $M_s$ ) of 31 kA/m<sup>50</sup> due to the proximity to its compensation temperature of 220 K, and exhibits a perpendicular magnetic anisotropy resulting from magnetostriction, e.g., with an anisotropy field of 0.53 T in our earlier work<sup>25</sup>. In contrast, YIG also forms a polycrystalline film on Si, but its small negative magnetostriction coefficients yield  $\lambda_s$  = -2.14x10<sup>-649</sup>. As a result of the smaller magnetoelastic anisotropy and larger  $M_s$  compared to DyIG, films of YIG/Si do not exhibit PMA. By substituting Dy for Y, the anisotropy and  $M_s$  can be tuned over a wide range. A composition of Y<sub>1.25</sub>Dy<sub>1.75</sub>Fe<sub>5</sub>O<sub>12</sub> (YDyIG) forms a PMA film on Si with lower coercivity and higher M<sub>s</sub> than that of DyIG<sup>48</sup> and was selected for this work. The lower coercivity composition was selected to make the effects of voltage-induced strain more prominent.

Films of 42 nm thick YDyIG/Si crystallized as single-phase garnet with no secondary phases, Figure 1(a). Hysteresis loops, Figure 1(b), show an OP easy axis,  $M_s$  of 60 kA/m, and coercivity  $\mu_0 H_C = 75$ mT. However, films grown and annealed directly on a PMN-PT substrate produced peaks characteristic of an orthoferrite film, (Y,Dy)FeO<sub>3</sub>, Figure 1(a). The orthoferrite forms due to epitaxial growth on the perovskite-structured PMN-PT despite the (Y,Dy):Fe ratio of 0.6 instead of 1, the value for a stoichiometric orthoferrite. As a comparison, films grown from a YIG target similarly formed yttrium orthoferrite on a SrTiO<sub>3</sub> substrate<sup>51</sup> due to epitaxial stabilization of the orthoferrite. A barrier layer is therefore required to prevent epitaxial growth, and this was provided by 5 nm amorphous silica. Grazing incidence X-ray diffraction (GIXD) of the 42 nm YDyIG/5 nm SiO<sub>2</sub>/PMN-PT after crystallization, Figure 1(a), shows single phase polycrystalline garnet peaks, confirming the effectiveness of the silica barrier.

Grain structure and surface topography were investigated via image-quality electron backscatter diffraction (IQ-EBSD) and atomic force microscopy (AFM) images. IQ-EBSD is shown in Figures 2(a,b) for YDyIG/Si and in Figure 2(c,d) for YDyIG/SiO<sub>2</sub>/PMN-PT. The grains in these films are around 5  $\mu m$  in size. Each grain shows a pattern of radiating lines which are attributed to low angle grain boundaries that form as the advancing crystallization front becomes unstable.<sup>48</sup> Surface topography of the uncoated Si substrate shows a sub-0.1 nm average roughness, whereas the uncoated PMN-PT substrate, Figure 3(a), has a roughness  $R_a = 0.83$  nm. This roughness is attributed to the ferroelectric domain structure and associated height differences in the piezoelectric substrate. Deposition of the 5 nm silica layer does not affect the roughness, but it leads to a reduction in the length scale of the domains, Figure 3(b). Since this change precedes our magnetometry measurements, it does not affect our results. After the final 42 nm of YDyIG is deposited and annealed, ≈100 nm-sized features are evident over the domain structure in Figure 3(c), and the roughness increases to 1.41 nm. The grain boundaries and radiating features within the grains can be seen in the higher magnification AFM images, Figure 3(d). The YDyIG on both substrates therefore consists of large plate-like grains (≈5 µm diameter, 42 nm thick) with random crystallographic orientation.

The magnetic hysteresis loops of YDvIG/SiO<sub>2</sub>/PMN-PT, Figure 1(c), show  $M_s = 60$  kA/m, and coercivity  $\mu_0 H_C = 20$  mT for both IP and OP directions. The anisotropy was determined from the

PLEASE CITE THIS ARTICLE AS DOI: 10.1063/5.0128842

area between the anhysteretic IP and OP curves.  $^{21}$  The YDyIG/SiO<sub>2</sub>/PMN-PT sample in Figure 1(c) is nearly isotropic, but the saturation field is slightly lower in the OP direction. We calculate a weak net anisotropy  $K_{\text{net}} = (750\pm10) \text{ J/m}^3$  (error bar reflects one-sigma uncertainty of the estimated value) with an OP easy axis, and the calculated anisotropy field is  $\mu_0 H_k = 2K_{\text{net}}/M_s = 25$  mT. The shape anisotropy  $^{52}$  ( $\mu_0 M_s^2/2$ ) contributes -(3200±10) J/m³, implying that the magnetoelastic anisotropy is (3950±20) J/m³. Growth induced anisotropy is not considered here since the film is annealed after the deposition, eliminating any structural or chemical ordering, and magnetocrystalline anisotropy is neglected because the film is polycrystalline. Following the same process, the calculated magnetoelastic anisotropy of YDyIG/Si is (5900±20) J/m³. The lower anisotropy of YDyIG/SiO<sub>2</sub>/PMN-PT vs. YDyIG/Si suggests a lower tensile strain in the former sample. PMN-PT undergoes several structural changes between room temperature and 750 °C  $^{53}$ , i.e., its thermal expansion is not linear, but above 200 °C its thermal expansion is slightly larger than that of Si,  $\alpha_{\text{PMN-PT}} = 5 \times 10^{-6} \text{ K}^{-1.54} \text{ vs. } \alpha_{\text{Si}} = 4 \times 10^{-6} \text{ K}^{-1.55} \text{ at } 200 \text{ °C}$ , which would reduce the thermal mismatch strain and anisotropy of YDyIG/SiO<sub>2</sub>/PMN-PT. The 5 nm silica layer has negligible effects on the strain state due to its small thickness.

The anisotropy of YDyIG/SiO<sub>2</sub>/PMN-PT was modulated via the piezoelectric deformation of the substrate (Supplementary Materials). For convenience we refer to the orthogonal IP substrate directions  $\hat{a}_1$  = [100] and  $\hat{a}_2$  = [01 $\bar{1}$ ], and the OP direction  $\hat{a}_3$  = [011]. Hysteresis loops were measured both before and after poling in all three directions  $\hat{a}_1$ ,  $\hat{a}_2$ , and  $\hat{a}_3$ . Figure 4(a) gives the loops in the unpoled state for a 5 mm x 5 mm sample that was cut from the same substrate as the sample in Figure 1(c). The sample of Figure 4(a) had an IP easy axis in the unpoled state with coercivity  $\mu_0 H_C = 20$  mT,  $M_s = 71$  kA/m, and anisotropy of  $K_{\rm net} \approx 300$  J m<sup>-3</sup> between the IP and OP directions. The difference between the two samples, Figs. 1(c) and 4(a), is attributed to a non-uniform film growth across the 10 mm x 10 mm area of film deposition, and/or strain relaxation during sample cutting or processing the electrodes.

Figures 4(b-d) show the hysteresis loops after applying a poling voltage of (150, 300, and 450) V respectively and then measuring the hysteresis at zero voltage. The magnetic anisotropy is changed in a nonvolatile manner by poling, and that poling breaks the symmetry between the  $\hat{a}_1$  and  $\hat{a}_2$  IP directions. Table I shows the magnetic anisotropy energies determined from the anhysteretic curves. Increasing the poling voltage makes the  $\hat{a}_3$  [011] the hardest and  $\hat{a}_2$  [01 $\bar{1}$ ] the easiest direction of magnetization, with  $\hat{a}_1$  [100] an intermediate axis. To confirm the results, the same measurements were conducted on an additional sample (see Figure S1 and Table S1), yielding similar trends in anisotropy.

	$K_{12}$ , J m <sup>-3</sup>	K <sub>31,</sub> J m <sup>-3</sup>	K <sub>32,</sub> J m <sup>-3</sup>	$\epsilon_{11}$ , 10 <sup>-6</sup>	$\epsilon_{22}$ , 10 <sup>-6</sup>
0 V (DEPOLED)	207 ± 16	2865	3072	1140 ± 10	1290
150 V	469	2270	1801	1010	660
300 V	568	2679	2111	1190	770
450 V (POLED)	826	2186	1360	1040	420

This is the author's peer reviewed, accepted manuscript. However, the online version of record will be different from this version once it has been copyedited and typeset PLEASE CITE THIS ARTICLE AS DOI: 10.1063/5.0128842

Applying a voltage along the [011] direction of the (011)-oriented PMN-PT generates a strain (denoted  $\epsilon_{ii}$ , referring to coordinate axes  $\hat{a}_i$ ) such that  $\epsilon_{11} \neq \epsilon_{22}$  leading to a difference in magnetic anisotropy energy along  $\hat{a}_1$  and  $\hat{a}_2$ , the in-plane directions. Considering only magnetoelastic anisotropy and shape anisotropy contributions, the anisotropy may be written (see Supplementary Materials)

$$K_{12} = \frac{3}{2} \lambda_s \frac{E}{1+\nu} (\epsilon_{11} - \epsilon_{22})$$
 [1]

$$K_{31} = \frac{\mu_0}{2} M_s^2 - \frac{3}{2} \lambda_s \frac{E}{1 - \nu^2} (\epsilon_{22} - \nu \epsilon_{11})$$
 [2]

$$K_{32} = \frac{\mu_0}{2} M_S^2 - \frac{3}{2} \lambda_S \frac{1}{1 - \nu^2} (\epsilon_{11} - \nu \epsilon_{22})$$
 [3]

(see Supplementary Materials)  $K_{12} = \frac{3}{2}\lambda_S \frac{E}{1+\nu}(\epsilon_{11} - \epsilon_{22}) \qquad [1]$   $K_{31} = \frac{\mu_0}{2}M_S^2 - \frac{3}{2}\lambda_S \frac{E}{1-\nu^2}(\epsilon_{22} - \nu\epsilon_{11}) \qquad [2]$   $K_{32} = \frac{\mu_0}{2}M_S^2 - \frac{3}{2}\lambda_S \frac{E}{1-\nu^2}(\epsilon_{11} - \nu\epsilon_{22}) \qquad [3]$ where  $K_{ij}$  is the magnetic anisotropy between directions i and j. Eq [1] represents the IP anisotropy. The shape anisotropy presented in Eqs. [2] and [3] is  $\frac{\mu_0}{2}M_S^2$  = (3170±6) J m<sup>-3</sup>. E is the elastic modulus of the film = 200 GPa,  $\nu$  is Poisson's ratio = 0.29, and  $\lambda_s$  is the magnetostriction coefficient of polycrystalline YDyIG $^{56}$ . From the Y:Dy ratio of the sample,  $\lambda_s$  of YDyIG is interpolated as  $0.417\lambda_{s,YIG}+0.583\lambda_{s,DyIG}=-5.87x10^{-6}$ . Substituting these values and solving Eqs. [1-3] yields the calculated tensile strain states  $\epsilon_{11}$  and  $\epsilon_{22}$  shown in Table I. Increasing the poling voltage has little effect on  $\epsilon_{11}$ , but reduces the magnitude of  $\epsilon_{22}$ , making  $\hat{a}_2$  an easier axis compared to  $\hat{a}_1$ .

Remanent strain generated by poling the (011)-oriented PMN-PT is dictated by the change in the domain configuration caused by poling then relaxing the electric field. The bulk PMN-PT is rhombohedral but has a composition near the morphotropic phase boundary. In the rhombohedral phase the polarization lies along the <111> directions. After growth and annealing of the garnet film, the unpoled substrate is expected to exhibit domains of all eight variants as it cools through its phase transformation temperatures. Four of the domains have polarization IP with components along  $\hat{a}_1$  and  $\hat{a}_2$  (i.e.,  $[11\bar{1}]$ ,  $[1\bar{1}1]$ ,  $[\bar{1}1\bar{1}]$  and  $[\bar{1}11]$ ) and the other four have an OP component along  $\hat{a}_3$  and IP along  $\hat{a}_1$ , but no component along  $\hat{a}_2$  (i.e., [111], [ $\bar{1}11$ ], [1 $\bar{1}\bar{1}$ ] and  $[\overline{1}\overline{1}\overline{1}]^{57}$ . Applying an OP voltage selects the two domains with components of polarization parallel to the electric field ([111] and [ $\overline{1}$ 11] for a field along  $+\hat{a}_3$ ), and after the field is removed the sample has an increased or a dominant population of those domains. The reduction or elimination of domains with polarization components along  $\hat{a}_2$  causes a compressive strain in the  $\hat{a}_2$  direction which is non-volatile. This explains the reduction in the tensile strain  $\epsilon_{22}$  in the YDyIG, whereas the strain  $\epsilon_{11}$  is little affected.

The data (Table I) shows an increasing anisotropy with poling voltage, though the 300 V measurement does not fit a monotonic trend. We therefore focus on the 450 V data to analyze strain changes resulting from poling. Although the volume fractions of the differently oriented ferroelectric domains at remanence is not known, we can estimate an upper bound for the change in strain of  $1300 \times 10^{-6}$  along  $\hat{a}_2$  corresponding to reorientation of half the domains (those

PLEASE CITE THIS ARTICLE AS DOI: 10.1063/5.0128842

with IP polarization) into the favored [111] and [ $\overline{1}$ 11] domains<sup>57</sup>. This is in reasonable agreement with the strain change of (870±20)x10<sup>-6</sup> along  $\hat{a}_2$  deduced from the anisotropy measurements of the sample after poling with 450 V.

The magnetoelectric coupling may be estimated from the electric field E (450 V divided by the thickness of the substrate, 500  $\mu m$ , i.e.,  $\mathcal{E} = 9 \times 10^5 \text{ V m}^{-1}$ ) and the resulting change in magnetic properties. Using a definition of converse magnetoelectric coefficient based on the change in magnetization with electric field  $\alpha_{me}$  =  $\mu_0(dM/dE)^{58}$ , where dM is taken as the change in remanent magnetization, the largest change in M is  $\approx 20$  kA/m at 450 V. This yields  $\alpha_{\rm me} = 2.8 \times 10^{-}$ <sup>7</sup> s m<sup>-1</sup>, similar to values reported for FeRh alloys on PMN-PT of (2 to 10)x10<sup>-7</sup> s m<sup>-1</sup> s m<sup>-1</sup> smaller than that of FeGa/PMN-PT (2.7x10 $^{-6}$  s m $^{-1}$ ) $^{61}$ , FeRh/BaTiO $_3$  (1.6x10 $^{-5}$  s m $^{-1}$ ) $^{62}$  and Co<sub>2</sub>FeSi/PMN-PT (1x10<sup>-5</sup> s m<sup>-1</sup>)<sup>63</sup>, all of which involve metallic magnetic films. Considering magnetic oxide films on ferroelectric substrates, La<sub>0.7</sub>Sr<sub>0.3</sub>MnO<sub>3</sub>/PMN-PT yielded  $\alpha_{me}$  = 6.4x10<sup>-8</sup> s m<sup>-164</sup> and YIG/PMN-PZT yielded a maximum  $\alpha_{\rm me} = 1.8 \times 10^{-7}$  s m<sup>-1 65</sup>, smaller than the present result. Alternatively, a magnetoelectric coefficient can also be defined as the change in anisotropy field (H<sub>K</sub>) with electric field,  $\alpha'_{me} = \mu_0(dH_K/dE)$ . The biggest change in anisotropy between poled and unpoled states is  $\Delta K_{32}$  = 1712 J m<sup>-3</sup> corresponding to a 48.2 mT change in  $\mu_0 H_K$ . The magnetoelectric coefficient is then  $\alpha'_{me}$  = 5.4x10<sup>-8</sup> s m<sup>-1</sup>. This is larger than values reported for the change in anisotropy field by ferromagnetic resonance for 4.9  $\mu m$  YIG/PMN-PT, yielding  $\alpha'_{me}$  = 5.4x10<sup>-9</sup> s m<sup>-166</sup>, or for 10-40  $\mu$ m YIG-PZT with  $\alpha'_{me}$  = 1-1.5x10<sup>-9</sup> s m<sup>-167</sup>.

In summary, we demonstrate nonvolatile voltage-tunable anisotropy from converse magnetoelectric coupling in a RE garnet film grown directly on a piezoelectric substrate. We first demonstrated the growth of single-phase polycrystalline garnet,  $Y_{1.25}Dy_{1.75}Fe_5O_{12}$  (YDyIG), on a (011)-oriented PMN-PT substrate by PLD followed by rapid thermal annealing at 750 °C, using a 5 nm silica barrier layer to prevent the formation of epitaxial orthoferrite phases. The 42 nm thick annealed YDyIG film consists of randomly oriented grains of  $\approx$ 5  $\mu$ m diameter with internal radially oriented low angle grain boundaries. The magnetic hysteresis curves indicate the presence of a perpendicular magnetic anisotropy contribution due to tensile thermal mismatch strain in the garnet combined with its negative magnetostriction.

Poling the substrate with an OP electric field leads to a reduction in the tensile strain along the  $[01\overline{1}]$  IP direction. The film acquired an easy axis along  $[01\overline{1}]$  and an intermediate axis along [100] with the OP direction [011] the hard axis. The change in anisotropy of the YDylG film is in reasonable agreement with the expected change in strain and the estimated magnetostriction coefficient of the YDylG. The converse magnetoelectric coupling is larger than or comparable to other reports of magnetic oxide films on ferroelectric substrates. The active control of anisotropy via voltage in a rare earth garnet is a useful step towards the development of magnetoelectric spintronic devices.

## **Supplementary Material**

See Supplementary Material for the calculation of anisotropy from biaxial strain and details of growth and characterization methods.

PLEASE CITE THIS ARTICLE AS DOI: 10.1063/5.0128842

**Author's Contributions** 

Jayasimha Atulasimha: conceptualization (equal); review and editing (equal). Dhritiman Bhattacharya: conceptualization (supporting). Daniel B. Gopman: review and editing (equal); conceptualization (equal). Miela J. Gross: conceptualization (equal); writing original draft (lead); formal analysis (lead); review and editing (equal). Kensuke Hayashi: formal analysis (supporting); review and editing (supporting). Walid A. Misba: conceptualization (equal); writing original draft (supporting); formal analysis (equal). Caroline A. Ross: conceptualization (equal); review and editing (lead).

## Acknowledgements

C.A.R. and M.G. acknowledge the support of the National Science Foundation Award DMR1954606; SMART, an nCORE Center of SRC; and the use of shared experimental facilities of the Center for Materials Science and Engineering, a Materials Research Science and Engineering Center (MRSEC) supported by NSF Award DMR1419807. W.A.M and J.A. acknowledge funding from NSF Award ECCS 1954589 and use of Nanocore Characterization Center (NCC) and Virginia Microelectronics Center (VMC) at VCU. The authors thank A. Kossak (MIT) for SiO<sub>2</sub> film growth.

## **Data Availability Statement**

The data that support the findings of this study are available from the corresponding author upon reasonable request.

PLEASE CITE THIS ARTICLE AS DOI: 10.1063/5.0128842

## **Figures**

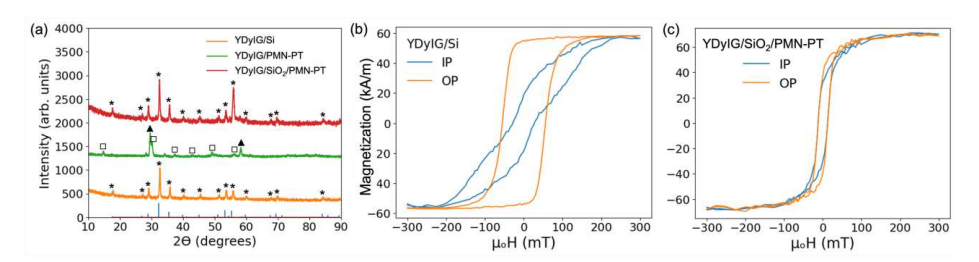


**Figure 1.** (a) GIXD of YDyIG/Si (orange), YDyIG/PMN-PT (green), and YDyIG/SiO $_2$ /PMN-PT (red). Data has been vertically shifted for clarity. Orthoferrite and substrate peaks are labeled with boxes and black triangles respectively. Garnet reference peaks are plotted as blue bars on the horizontal axis and are labeled with black stars on the scans. (b,c) Magnetic hysteresis loops measured IP and OP of 41.6 nm thick YDyIG on (b) Si and (c) SiO $_2$ /PMN-PT.

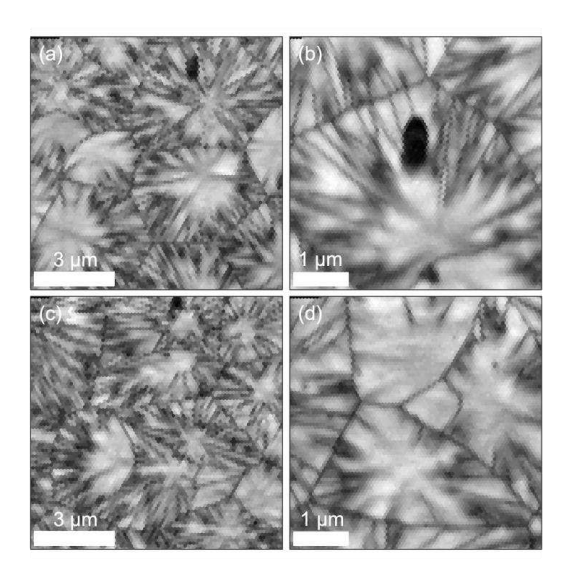


**Figure 2.** EBSD IQ-Images of (a,b) YDyIG/Si and (c,d) YDyIG/SiO<sub>2</sub>/PMN-PT. Images (a,c) are 10  $\mu$ m x 10  $\mu$ m and images (b,d) are 5  $\mu$ m x 5  $\mu$ m. Both samples show grains roughly 5  $\mu$ m in diameter with radiating contrast attributed to low angle grain boundaries.

PLEASE CITE THIS ARTICLE AS DOI: 10.1063/5.0128842

(a) R<sub>3</sub> 0.8 nn (b) R<sub>3</sub> 1.3 nm (c) R<sub>3</sub> 1.4 nm (d)

**Figure 3.** AFM images of surface topography at different stages of heterostructure growth. (a) PMN-PT substrate, (b) 5nm SiO<sub>2</sub>/PMN-PT, and (c) 42 nm YDyIG/SiO<sub>2</sub>/PMN-PT. (a-c) are all 5  $\mu$ m x 5 $\mu$ m in size; (d) 2  $\mu$ m x 2  $\mu$ m of 42 nm YDyIG/SiO<sub>2</sub>/PMN-PT, where grain boundaries exhibit faint contrast. Average roughness  $R_a$  is labelled.

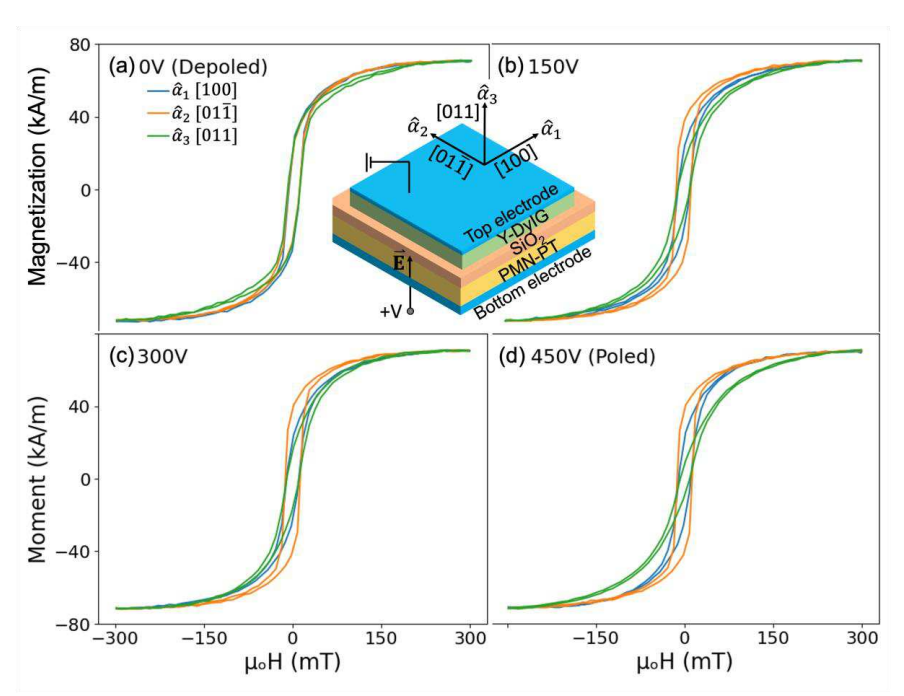


**Figure 4.** Hysteresis loops of YDyIG/SiO<sub>2</sub>/PMN-PT measured in all three principal directions, (a) unpoled and (b-d) after poling at different voltages then removing the electric field. Inset shows the poling configuration with both top and bottom electrodes. The device is poled along the [011] OP direction. The direction of the applied external field is indicated with plot colors in the legend of (a).

## PLEASE CITE THIS ARTICLE AS DOI: 10.1063/5.0128842

This is the author's peer reviewed, accepted manuscript. However, the online version of record will be different from this version once it has been copyedited and typeset

## References

- <sup>1</sup> Y. Kajiwara, K. Harii, S. Takahashi, J. Ohe, K. Uchida, M. Mizuguchi, H. Umezawa, H. Kawai, K. Ando, K. Takanashi, S. Maekawa, and E. Saitoh, Nature **464**, 262 (2010).
- <sup>2</sup> M.A. Azam, D. Bhattacharya, D. Querlioz, C.A. Ross, and J. Atulasimha, Nanotechnology **31**, (2020).
- <sup>3</sup> C.O. Avci, A. Quindeau, M. Mann, C.F. Pai, C.A. Ross, and G.S.D. Beach, Phys Rev B **95**, 115428 (2017).
- <sup>4</sup> Y. Yang, T. Liu, L. Bi, and L. Deng, J Alloys Compd **860**, 158235 (2021).
- <sup>5</sup> L. Soumah, N. Beaulieu, L. Qassym, C. Carrétéro, E. Jacquet, R. Lebourgeois, J. ben Youssef, P. Bortolotti, V. Cros, and A. Anane, Nat Commun **9**, (2018).
- <sup>6</sup> H. Chang, P. Li, W. Zhang, T. Liu, A. Hoffmann, L. Deng, and M. Wu, IEEE Magn Lett 5, 1 (2014).
- <sup>7</sup> O. Ciubotariu, A. Semisalova, K. Lenz, and M. Albrecht, Sci Rep **9**, (2019).
- <sup>8</sup> C.O. Avci, E. Rosenberg, M. Baumgartner, L. Beran, A. Quindeau, P. Gambardella, C.A. Ross, and G.S.D. Beach, Appl Phys Lett **111**, 8 (2017).
- <sup>9</sup> J. Li, G. Yu, C. Tang, Y. Liu, Z. Shi, Y. Liu, A. Navabi, M. Aldosary, Q. Shao, K.L. Wang, R. Lake, and J. Shi, Phys Rev B 95, 1 (2017).
- <sup>10</sup> Y. Lin, L. Jin, H. Zhang, Z. Zhong, Q. Yang, Y. Rao, and M. Li, J Magn Magn Mater 496, 165886 (2020).
- <sup>11</sup> T. Fakhrul, S. Tazlaru, L. Beran, Y. Zhang, M. Veis, and C.A. Ross, Adv Opt Mater **7**, 1 (2019).
- <sup>12</sup> T. Fakhrul, S. Tazlaru, B. Khurana, L. Beran, J. Bauer, M. Vančík, A. Marchese, E. Tsotsos, M. Kučera, Y. Zhang, M. Veis, and C.A. Ross, Adv Opt Mater 9, 2100512 (2021).
- <sup>13</sup> L. Caretta, E. Rosenberg, F. Büttner, T. Fakhrul, P. Gargiani, M. Valvidares, Z. Chen, P. Reddy, D.A. Muller, C.A. Ross, and G.S.D. Beach, Nat Commun 11, 1 (2020).
- <sup>14</sup> A.J. Lee, S. Guo, J. Flores, B. Wang, N. Bagués, D.W. McComb, and F. Yang, Nano Lett 20, 4667 (2020).
- <sup>15</sup> S. Xia, S. Zhang, Z. Luan, L. Zhou, J. Liang, G. Liu, B. Yang, H. Yang, R. Liu, and D. Wu, Appl Phys Lett **116**, 052404 (2020).
- <sup>16</sup> S.G. Je, D.H. Kim, S.C. Yoo, B.C. Min, K.J. Lee, and S.B. Choe, Phys Rev B Condens Matter Mater Phys **88**, 1 (2013).
- <sup>17</sup> Y. Zhang, Q. Du, C. Wang, W. Yan, L. Deng, J. Hu, C.A. Ross, and L. Bi, APL Mater 7, (2019).
- <sup>18</sup> J.J. Bauer, E.R. Rosenberg, and C.A. Ross, Appl Phys Lett **114**, 052403 (2019).
- <sup>19</sup> E.R. Rosenberg, K. Litzius, J.M. Shaw, G.A. Riley, G.S.D. Beach, H.T. Nembach, and C.A. Ross, Adv Electron Mater **7**, 2100452 (2021).
- <sup>20</sup> C.O. Avci, E. Rosenberg, M. Huang, J. Bauer, C.A. Ross, and G.S.D. Beach, Phys Rev Lett 124, 027701 (2020).
- <sup>21</sup> R.C. O'Handley, Physics Bulletin (1999).
- <sup>22</sup> D.B. Sirdeshmukh, K.G. Subhadra, K.A. Hussain, N.G. Krishna, and B.R. Rao, Crystal Research and Technology **28**, 15 (1993).
- <sup>23</sup> E.R. Rosenberg, L. Beran, C.O. Avci, C. Zeledon, B. Song, C. Gonzalez-Fuentes, J. Mendil, P. Gambardella, M. Veis, C. Garcia, G.S.D. Beach, and C.A. Ross, Phys Rev Mater **2**, (2018).
- <sup>24</sup> T. Bayaraa, C. Xu, D. Campbell, and L. Bellaiche, Phys Rev B **100**, 214412 (2019).
- <sup>25</sup> J.J. Bauer, E.R. Rosenberg, S. Kundu, K.A. Mkhoyan, P. Quarterman, A.J. Grutter, B.J. Kirby, J.A. Borchers, and C.A. Ross, Adv Electron Mater **6**, 1900820 (2020).

## PLEASE CITE THIS ARTICLE AS DOI: 10.1063/5.0128842

This is the author's peer reviewed, accepted manuscript. However, the online version of record will be different from this version once it has been copyedited and typeset

- <sup>26</sup> X.J. Chen, G. Perillat-Merceroz, D. Sam-Giao, C. Durand, and J. Eymery, Appl Phys Lett **97**, 151909 (2010).
- <sup>27</sup> X. Yang, Y. Gao, J. Wu, Z. Zhou, S. Beguhn, T. Nan, and N.X. Sun, IEEE Microwave and Wireless Components Letters **24**, 191 (2014).
- <sup>28</sup> T. Wu, A. Bur, K. Wong, J. Leon Hockel, C.J. Hsu, H.K.D. Kim, K.L. Wang, and G.P. Carman, J Appl Phys **109**, 07D732 (2011).
- <sup>29</sup> T. Wu, A. Bur, P. Zhao, K.P. Mohanchandra, K. Wong, K.L. Wang, C.S. Lynch, and G.P. Carman, Appl Phys Lett **98**, 012504 (2011).
- <sup>30</sup> I. Gilbert, A.C. Chavez, D.T. Pierce, J. Unguris, W.Y. Sun, C.Y. Liang, and G.P. Carman, Appl Phys Lett **109**, 162404 (2016).
- <sup>31</sup> Y. Xiang, K. Liang, S. Keller, M. Guevara, M. Sheng, Z. Yan, P. Zhou, Y. Qi, Z. Ma, Y. Liu, G. Srinivasan, G.P. Carman, T. Zhang, and C.S. Lynch, Smart Mater Struct **29**, 095019 (2020).
- <sup>32</sup> Q. Li, A. Tan, A. Scholl, A.T. Young, M. Yang, C. Hwang, A.T. N'Diaye, E. Arenholz, J. Li, and Z.Q. Qiu, Appl Phys Lett 110, (2017).
- <sup>33</sup> D.B. Gopman, P. Chen, J.W. Lau, A.C. Chavez, G.P. Carman, P. Finkel, M. Staruch, and R.D. Shull, ACS Appl Mater Interfaces **10**, 24725 (2018).
- <sup>34</sup> W. Zhou, C. Ma, Z. Gan, Z. Zhang, X. Wang, W. Tan, and D. Wang, Appl Phys Lett 111, 052401 (2017).
- <sup>35</sup> T. Shen, V. Ostwal, K.Y. Camsari, and J. Appenzeller, Sci Rep 10, (2020).
- <sup>36</sup> W. Liang, F. Hu, J. Zhang, H. Kuang, J. Li, J. Xiong, K. Qiao, J. Wang, J. Sun, and B. Shen, Nanoscale **11**, 246 (2019).
- <sup>37</sup> Y. Wang, N. Mehmood, Z. Hou, W. Mi, G. Zhou, X. Gao, and J. Liu, Adv Electron Mater **8**, 2100561 (2022).
- <sup>38</sup> M. Liu, J. Hoffman, J. Wang, J. Zhang, B. Nelson-Cheeseman, and A. Bhattacharya, Sci Rep **3** (2013).
- **3**, (2013).

  <sup>39</sup> J. Lian, F. Ponchel, N. Tiercelin, Y. Chen, D. Rémiens, T. Lasri, G. Wang, P. Pernod, W. Zhang, and X. Dong, Appl Phys Lett **112**, 162904 (2018).
- <sup>40</sup> L. Han, F. Ponchel, D. Rémiens, T. Lasri, N. Tiercelin, G. Wang, and P. Pernod, J Appl Phys **126**, 164104 (2019).
- <sup>41</sup> R. Yu, K. He, Q. Liu, X. Gan, B. Miao, L. Sun, J. Du, H. Cai, X. Wu, M. Wu, and H. Ding, Adv Electron Mater **5**, 1800663 (2019).
- <sup>42</sup> R. Duflou, F. Ciubotaru, A. Vaysset, M. Heyns, B. Sorée, I.P. Radu, and C. Adelmann, Appl Phys Lett **111**, 192411 (2017).
- <sup>43</sup> Y. Zhou, T. Guo, L. Qiao, Q. Wang, M. Zhu, J. Zhang, Q. Liu, M. Zhao, C. Wan, W. He, H. Bai, L. Han, L. Huang, R. Chen, Y. Zhao, X. Han, F. Pan, and C. Song, Nano Lett 22, 4646 (2022).
- <sup>44</sup> T.C. Fung, A.D. Karenowska, and J.F. Gregg, Materials for Quantum Technology **1**, 011003 (2021).
- <sup>45</sup> Y. Zhao, Y. Li, S. Zhu, C. Chen, M. Yao, Y. Zhao, Z. Hu, B. Peng, M. Liu, and Z. Zhou, J Phys D Appl Phys **54**, 245002 (2021).
- <sup>46</sup> T. Su, S. Ning, E. Cho, and C.A. Ross, Phys Rev Mater **5**, 094403 (2021).
- <sup>47</sup> H.S. Kum, H. Lee, S. Kim, S. Lindemann, W. Kong, K. Qiao, P. Chen, J. Irwin, J.H. Lee, S. Xie, S. Subramanian, J. Shim, S.H. Bae, C. Choi, L. Ranno, S. Seo, S. Lee, J. Bauer, H. Li, K. Lee, J.A. Robinson, C.A. Ross, D.G. Schlom, M.S. Rzchowski, C.B. Eom, and J. Kim, Nature **578**, 75 (2020).

PLEASE CITE THIS ARTICLE AS DOI: 10.1063/5.0128842

## AIP Publishing

<sup>48</sup> M.J. Gross, J.J. Bauer, S. Ghosh, S. Kundu, K. Hayashi, E.R. Rosenberg, K. Andre Mkhoyan, and C.A. Ross, J Magn Magn Mater **564**, 170043 (2022).

<sup>49</sup> S. Iida, J Physical Soc Japan **22**, 1201 (1967).

<sup>50</sup> A. Paoletti, *Physics of Magnetic Garnets* (North-Holland Pub. Co., Amsterdam, 1979).

<sup>51</sup> S. Ning, A. Kumar, K. Klyukin, E. Cho, J.H. Kim, T. Su, H.S. Kim, J.M. LeBeau, B. Yildiz, and C.A. Ross, Nat Commun **12**, (2021).

<sup>52</sup> B.D. Cullity and C.D. Graham, *Introduction to Magnetic Materials* (2009).

<sup>53</sup> D. Lin, C. Li, S. Ge, E. Gorzkowski, S. Zhou, W. Liu, and F. Li, J Eur Ceram Soc 39, 2082 (2019).

<sup>54</sup> R. Wongmaneerung, R. Guo, A. Bhalla, R. Yimnirun, and S. Ananta, J Alloys Compd 461, 565 (2008).

<sup>55</sup> Y. Okada and Y. Tokumaru, J Appl Phys **56**, 314 (1984).

<sup>56</sup> H.M. Chou and E.D. Case, J Mater Sci Lett **7**, 1217 (1988).

<sup>57</sup> T. Wu, P. Zhao, M. Bao, A. Bur, J.L. Hockel, K. Wong, K.P. Mohanchandra, C.S. Lynch, and G.P. Carman, J Appl Phys **109**, 124101 (2011).

<sup>58</sup> W. Griggs and T. Thomson, Sci Rep **12**, (2022).

<sup>59</sup> I. Fina, A. Quintana, X. Martí, F. Sánchez, M. Foerster, L. Aballe, J. Sort, and J. Fontcuberta, Appl Phys Lett **113**, 152901 (2018).

<sup>60</sup> Q.B. Hu, J. Li, C.C. Wang, Z.J. Zhou, Q.Q. Cao, T.J. Zhou, D.H. Wang, and Y.W. Du, Appl Phys Lett 110, 222408 (2017).

<sup>61</sup> W. Jahjah, J.P. Jay, Y. le Grand, A. Fessant, A.R.E. Prinsloo, C.J. Sheppard, D.T. Dekadjevi, and D. Spenato, Phys Rev Appl **13**, 034015 (2020).

<sup>62</sup> R.O. Cherifi, V. Ivanovskaya, L.C. Phillips, A. Zobelli, I.C. Infante, E. Jacquet, V. Garcia, S. Fusil, P.R. Briddon, N. Guiblin, A. Mougin, A.A. Ünal, F. Kronast, S. Valencia, B. Dkhil, A. Barthélémy, and M. Bibes, Nat Mater 13, 345 (2014).

<sup>63</sup> S. Fujii, T. Usami, Y. Shiratsuchi, A.M. Kerrigan, A.M. Yatmeidhy, S. Yamada, T. Kanashima, R. Nakatani, V.K. Lazarov, T. Oguchi, Y. Gohda, and K. Hamaya, NPG Asia Mater 14, (2022).

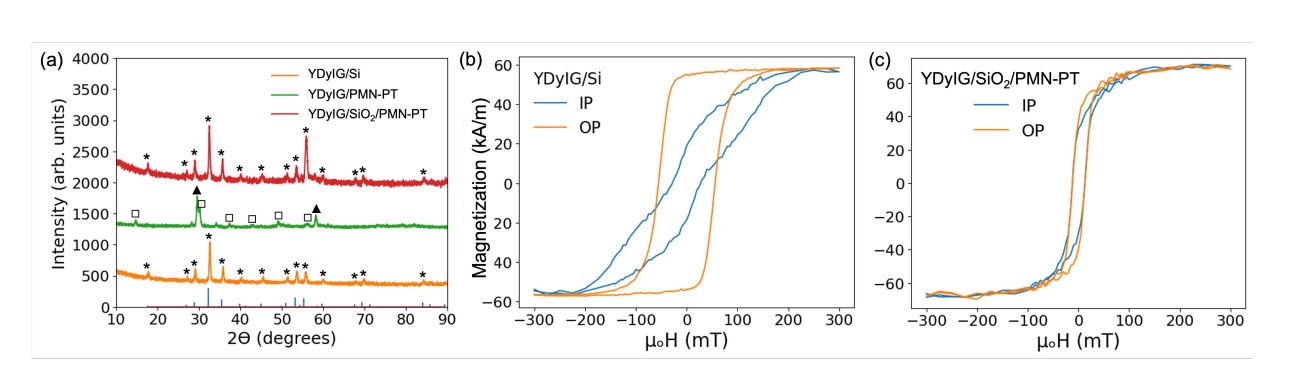
<sup>64</sup> D. Pesquera, E. Khestanova, M. Ghidini, S. Zhang, A.P. Rooney, F. Maccherozzi, P. Riego, S. Farokhipoor, J. Kim, X. Moya, M.E. Vickers, N.A. Stelmashenko, S.J. Haigh, S.S. Dhesi, and N.D. Mathur, Nat Commun 11, (2020).

<sup>65</sup> H. Liuyang, P. Freddy, R. Denis, L. Tuami, T. Nicolas, W. Genshui, and P. Philippe, Ferroelectrics **557**, 1 (2020).

<sup>66</sup> G. Srinivasan, M.I. Bichurin, and J. v. Mantese, Integrated Ferroelectrics **71**, 45 (2005).

<sup>67</sup> A.S. Tatarenko, V. Gheevarughese, G. Srinivasan, O. v. Antonenkov, and M.I. Bichurin, J Electroceram **24**, 5 (2010).

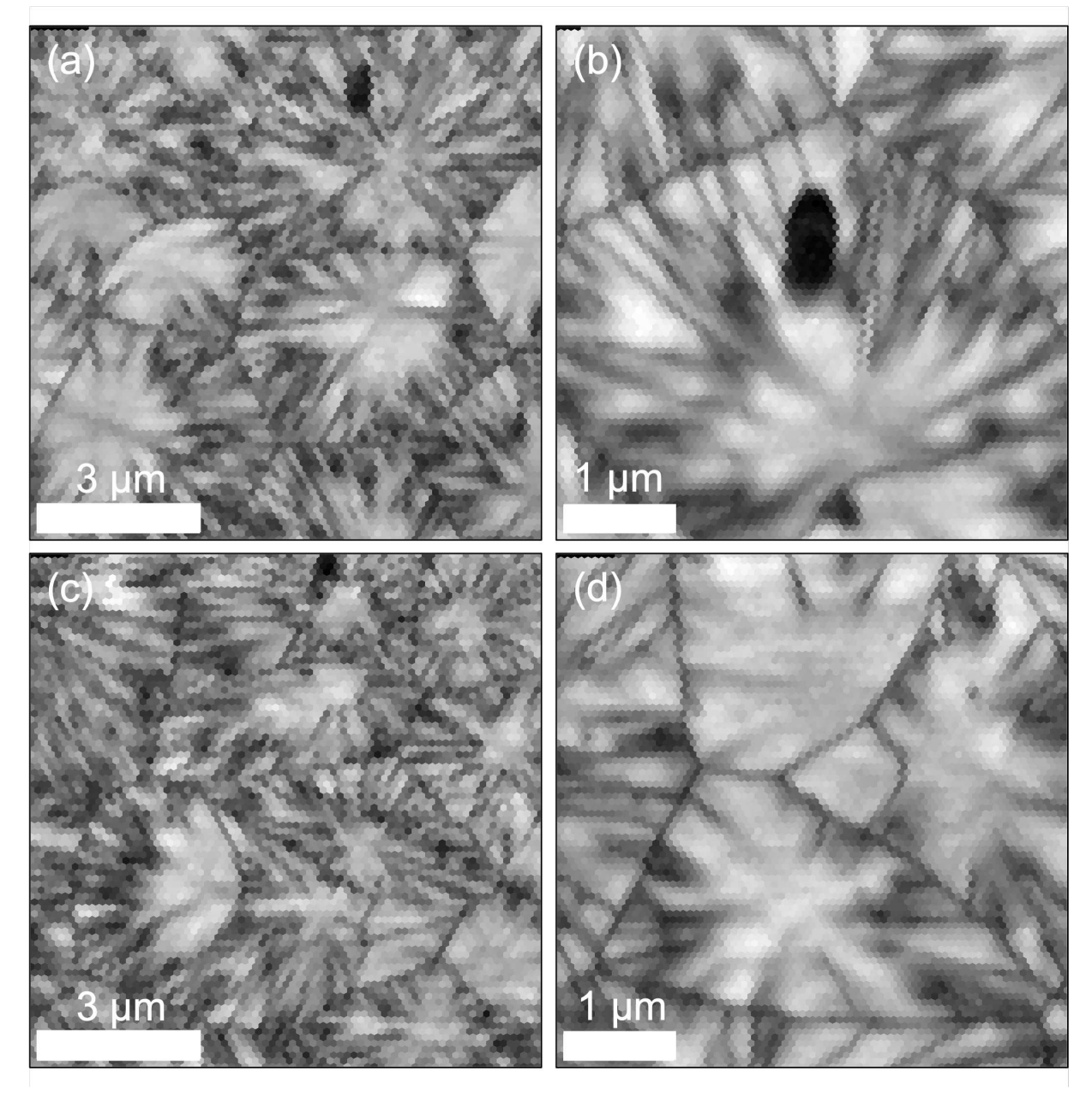




## **Applied Physics Letters**

## ACCEPTED MANUSCRIPT

This is the author's peer reviewed, accepted manuscript. However, the online version of record will be different from this version once it has been copyedited and typeset.

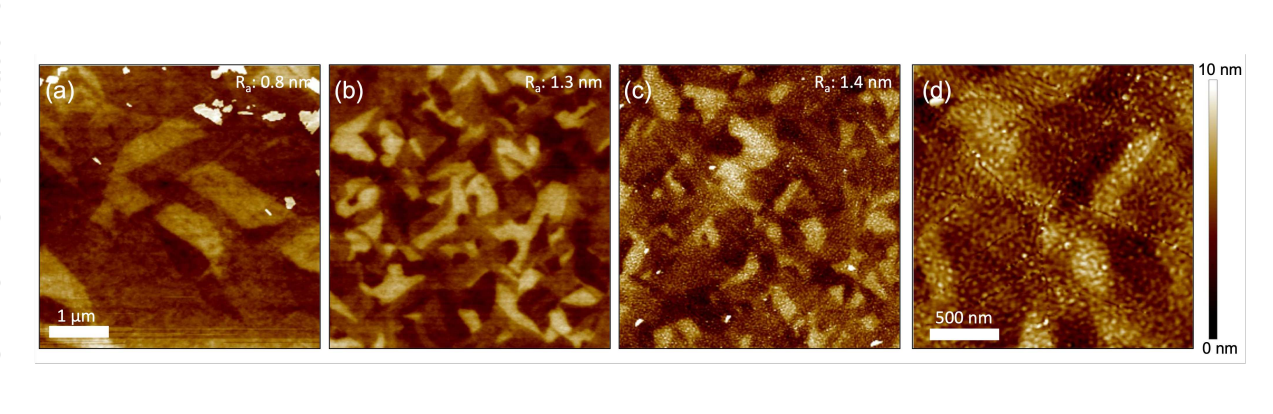




## **Applied Physics Letters**

## ACCEPTED MANUSCRIPT

This is the author's peer reviewed, accepted manuscript. However, the online version of record will be different from this version once it has been copyedited and typeset.



This is the author's peer reviewed, accepted manuscript. However, the online version of record will be different from this version once it has been copyedited and typeset.

